WFIRST Low Order Wavefront Sensing and Control Testbed Performance under Flight Like Photon Flux

Fang Shi, Byoung-Joon Seo, Eric Cady, Brian Kern, Raymond Lam, David Marx, Keith Patterson, Camilo Mejia Prada, John Shaw, Chris Shelton, Joel Shields, Hong Tang, Tuan Truong
Jet Propulsion Laboratory, California Institute of Technology
4800 Oak Grove Drive, Pasadena, USA, CA 91009, USA

ABSTRACT

To maintain the required performance for the WFIRST Coronagraph Instrument (CGI) in a realistic space environment, a Low Order Wavefront Sensing and Control (LOWFS/C) subsystem is necessary. The WFIRST CGI LOWFS/C subsystem would use the Zernike wavefront sensor, which has the phase-shifting disk combined with the coronagraph's focal plane mask, to sense the low-order wavefront drift and line-of-sight (LoS) error using the rejected starlight. The dynamic tests on JPL's on the Occulting Mask Coronagraph (OMC) Testbed have demonstrated that LOWFS/C can maintain coronagraph contrast to better than 10^{-8} in presence of WFIRST-like line of sight and low order wavefront disturbances in both Shaped Pupil Coronagraph (SPC) and Hybrid Lyot Coronagraph (HLC) modes. However, the previous dynamic tests have been done using a bright source with photon flux equivalent to stellar magnitude of Mv = -3.5. The LOWFS/C technology development continues on the OMC testbed especially in evaluating and improving the LOWFS/C performance under the realistic photon flux that is equivalent to WFIRST Coronagraph target stars. Our recent testbed tests have demonstrated that the LOWFS/C can work cohesively with the stellar light suppression wavefront control, which brings broad band coronagraph contrast from 1×10^{-6} to 6×10^{-9}, while LOWF/C is simultaneously suppressing the WFIRST like LoS and low order wavefront drift disturbances on a source that photon flux is equivalent to a Mv = 2 star. This demonstration mimics the CGI initial dark hole establish process on a bright reference star. We also demonstrated on the testbed that LOWFS/C can maintain the coronagraph contrast by suppressing the WFIRST like line-of-sight disturbances on a fainter Mv = 5 star. This mimics scenario of CGI science target observations. In this paper we will present the recent testbed results on LOWFS/C LoS loops and low order wavefront error correction loop performance on the flight like photon flux.

Keywords: WFIRST Coronagraph, Exoplanet, wavefront sensing and control, low order wavefront sensor, high contrast imaging, Zernike wavefront sensor, fast steering mirror, deformable mirror

1 INTRUDUCTION

1.1 Low order wavefront sensing and control for WFIRST CGI

A high contrast coronagraph instrument is very sensitive to the wavefront error [1, 2]. The WFIRST CGI requires the coronagraph to have raw contrast better than 10^{-8}. Additionally, in order to differentiate planets from residual speckles in the dark hole and to measure the planet with a proper signal-to-noise ratio, the coronagraph contrast needs to be stable at a level of $\sim10^{-9}$ during the observation. The contrast stability requirement drives a very tight tolerance for the wavefront error and line-of-sight jitter. In order to maintain the coronagraph contrast level and stability WFIRST CGI needs a low order wavefront sensing and control (LOWFS/C) subsystem. From the coronagraph performance requirements, the WFIRST LOWFS/C's sensor needs to have the LoS post correction residual less than 0.5 mas and low order wavefront error less than 0.25 nm rms [3].

The wavefront dynamics presented to the coronagraph consists of wavefront errors (WFE) in both the line-of-sight (wavefront tilt) error and low order wavefront aberrations such as focus, astigmatism, and coma. Depending on the sources of disturbances, these wavefront errors contain both low and high temporal frequency components, with the low frequency (sub Hz) WFE coming mostly from thermal load variation, and high frequency WFE from the vibration

© 2018 California Institute of Technology. Government sponsorship acknowledged.

disturbances such as the reaction wheel assemblies (RWA) used for WFIRST telescope pointing. The slow (< 2 Hz) LoS drift is from the telescope's attitude control system (ACS) residual pointing error. The WFIRST ACS requirement allows the telescope pointing error up to 14 milli-arcsecond rms (mas) per axis. The fast LoS jitter is caused by vibrations from the ACS's reaction wheels assemblies (RWA). Because the slow variation of RWA speed, the LoS jitter is tonal with fundamental frequency corresponding to the RWA's wheel speed. While the most of LoS jitter energy contains at the fundamental frequency, the LoS jitter does have multiple harmonic and sub-harmonic frequencies. WFIRST observatory requirement allows LoS jitter up to 14 mas per axis. During the coronagraph science observation, the spacecraft orbiting or telescope pointing will change the solar thermal load on the observatory, which will in turn cause the telescope's optics relative positions or surface figures to change. The integrated modeling of the WFIRST has shown that the thermally induced wavefront drift is about 0.5 nm rms. The dominant portion of the WFE are focus, caused by the telescope's optics position shifts from the thermal load variations. Higher aberration modes beyond spherical are all negligibly small, in single digit picometer. It is also evident that the wavefront drifts are very slow, typically under 0.001 Hz. We rely on the observatory modeling for the expected LoS and low order WFE disturbances [4].

WFIRST Coronagraph LOWFS/C sensor uses the rejected starlight reflected off the coronagraph's focal plane occulting mask for wavefront sensing. Figure 1 shows the WFIRST CGI's optical function diagram including LOWFS/C [15]. The LOWFS sensor is a Zernike wavefront sensor (ZWFS). The principle of ZWFS has been described in detail in our previously published papers [5]. One of the key features of WFIRST LOWFS/C design is that the Zernike wavefront sensor's phase shifting disk is designed and fabricated directly on the reflective side of the focal plane mask (FPM). In other words, the FPM has dual functions: coronagraph starlight suppression mask in transmission and LOWFS/C Zernike WFS mask in reflection. In this way, the starlight rejection and wavefront sensing occur at the same location. This not only ensures that the ZWFS measures WFE where the coronagraph needs but also avoids any significant non-common path error on ZWFS. The details of ZWFS mask design are different depending on the coronagraph mode [6, 7], but they all have the ZWFS phase shifting disk built in. For LOWFS/C the coronagraph's FPM acts as a low-pass spatial filter because of its limited size of the reflecting area, whose diameter is ~6 λ/D for HLC mask or ~5 λ/D for SPC mask. This low-pass filter nature causes the LOWFS/C Zernike wavefront sensor can only measure the low order wavefront error and is insensitive to mid and high spatial frequency WFE. Fortunately, the dominant WFIRST WFE drift and line-of-sight errors are low order in nature. The baseline WFIRST LOWFS/C ZWFS senses the first 11 low order Zernike terms: tilts (Z2, Z3), focus (Z4), astigmatisms (Z5, Z6), comas (Z7, Z8), trefoils (Z9, Z10), and spherical (Z11). A fixed 20% spectral filter centered at 550 nm is placed in front of the LOWFS/C camera. The baseline LOWFS/C camera uses the Teledyne E2V's EMCCD201, which will be modified for high frame rate of 1 KHz. The low order wavefront error, in the form of 10 Zernike coefficients (Z2-Z11), is computed at camera read out rate of 1 KHz.

The ZWFS sensed low order WFE is used to control corresponding wavefront correctors by the LOWFS/C, as shown in Figure 1. The sensed tip-tilt (Z2, Z3) is used to drive the Fast Steering Mirror (FSM) control loops at the command update rate of 1 KHz to suppress the LoS jitter and drift. Since the thermally induced WFE drift is very slow, the sensed low order WFE (Z4 – Z11) can be time-averaged over long period (minutes) to reduce the sensor noise without compromising the control bandwidth. The sensed focus term (Z4) is used to control the coronagraph's Focusing Mirror (FocM) which is an actuated fold flat mirror in a focused beam. Focus is the dominant mode of WFIRST WFE drifts so correcting it with the dedicated FocM will reduce the stroke burden on the deformable mirror. The rest of sensed low order wavefront error terms (Z5 – Z11), however, are used to drive DM1 for the correction.

In WFIRST Coronagraph, the role of LOWFS/C is to maintain the wavefront set by the HOWFS/C, which creates the coronagraph's dark hole at the beginning of a coronagraphic observation. The WFIRST LOWFS/C's sensor, therefore, works in the relative sensing mode, measuring the wavefront changes from the reference point set by HOWFS/C instead of measuring the absolute wavefront.

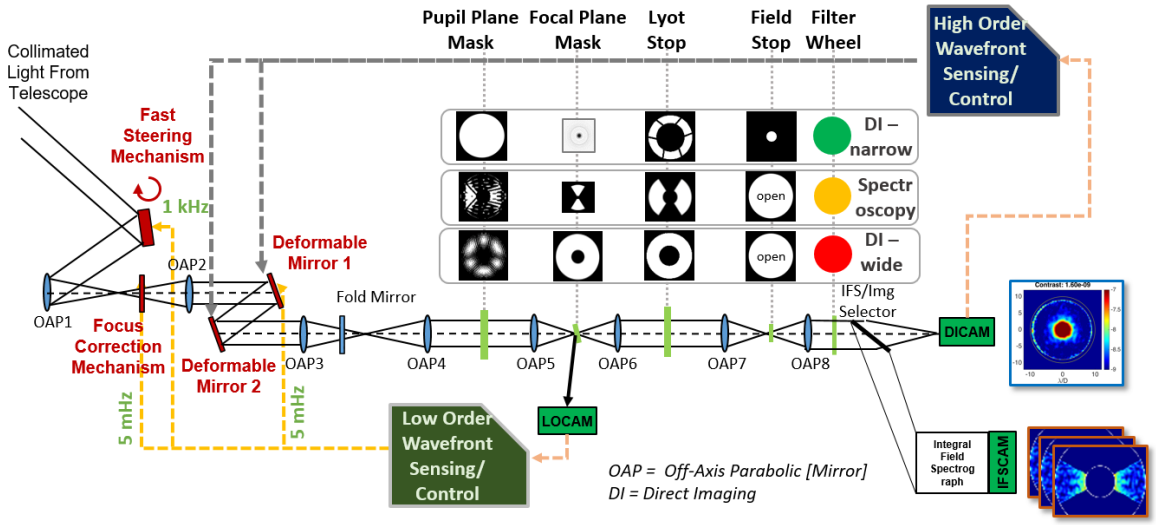

Figure 1. Functional illustration of WFIRST CGI and LOWFS/C. Starlight from the telescope and relay optics enters CGI instrument at left through the fast steering mirror (FSM) at a pupil plane. Relay optics are off-axis parabolas (OAP) which form various image or pupil planes for coronagraph masks and stops. Two deformable mirrors (DM1 conjugated to pupil and DM2) are used by high order wavefront control (HOWFS/C) to suppress the starlight for high contrast imaging. The WFIRST CGI can operate in either HLC, SPC spectrograph, or SPC wide field modes. The HLC masks and stops (top row) and SPC masks and stops (mid and bottom rows) are switched via mechanisms (indicated by vertical dash lines) at corresponding pupil and image planes. A selectable mirror sends coronagraph light to either the direct imaging camera (DICAM) or the integral field spectrograph camera (IFSCAM). The rejected starlight reflected off the focal plane mask, which has the LOWFS/C phase dimple built-in, is captured by the LOWFS/C optics that form a pupil image on the LOWFS/C camera (LOCAM). The LOWFS/C subsystem controls FSM, Focusing Correction Mirror (FocM), and DM1 with different updating frequencies as labeled in their corresponding control signal paths.

1.2 The FSM line-of-sight control loop

The WFIRST LoS line-of-sight control loops are unique which worth some description here. Figure 2 shows the schematic overview of the WFIRST LOWFS/C line-of-sight control loops. The LoS control has two branches, a feedback loop and a feedforward loop [8]. The feedback control loop is shaped to reduce the sensor noise and provide control bandwidth to correct the slow LoS drift from ACS. The feedback loop also provides line-of-sight targets to allow LoS offset when the loop is closed. The feedforward loop uses the knowledge of RWA wheel speed from ACS telemetry and dynamic model identified harmonic frequencies together with LOWFS sensor to cancel the RWA wheel induced the LoS jitter. The feedforward loop uses recursive least mean squares (LMS) fitting of the tones to determine control signals directly fed to FSM to suppress tonal LoS jitter excited by the RWA [12, 13]. The error transfer function from the feedforward loop is notch filters at the controlled frequencies. To increase LMS robustness against the RWA wheel speed knowledge multiple ringers next to each other have been implemented to the feedforward loop. As a matter of fact in the testbed we added two ringers to suppress the LoS jitters from the lab environment in addition to the ringer corresponding to the jitter from WFIRST disturbance.

The line-of-sight control uses the Fast Steering Mirror (FSM) with three PZT actuators and the design is inherited from the SIM project [9]. The FSM's PZT actuators have strain gauge sensors to close a local loop around the PZT displacements. This linearizes the hysteresis of the PZT and cancels any actuator drift or creep. To use the FSM for the feedforward control we need to have a good knowledge of the FSM transfer function. For the FSM used on testbed its tilt stroke, gain, linearity, and dynamic characteristics have been carefully measured and calibrated using various instruments such as Zygo, high-speed metrology system, and dynamometer [9]. These measurements and calibrations have been incorporated into the LoS control model.

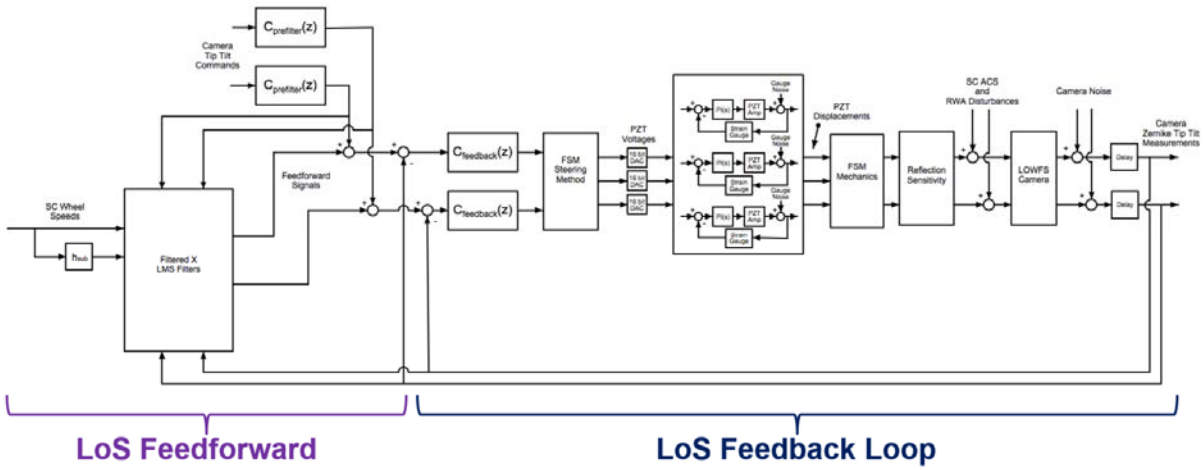

Figure 2. Block diagram depiction of the implemented line-of-sight drift and jitter compensation loops using a Fast Steering Mirror (FSM). The LoS control contains both the feedback loop and the feedforward loop. The control target inputs come in from the upper left and are filtered by $C_{prefilter}$. The ACS wheel speed input come from the left. The middle section is the FSM plant which has three PZT actuators and strain gauge local loops. The LOWFS camera and associated latency from frame grabber and computation are on the right. The WFE disturbances are introduced before the LOWFS camera.

1.3 Occulting mask coronagraph (OMC) testbed

To demonstrate the coronagraph performance under the WFIRST like dynamic environment we have built the Occulting Mask Coronagraph (OMC) testbed. The OMC testbed mimics the WFIRST CGI design and has both HLC and SPC coronagraph modes, a LOWFS/C subsystem, and later on, an integral field spectrograph (IFS). It also an Optical Telescope Assembly (OTA) Simulator, which is directly carried over from the LOWFS/C testbed, for WFE disturbances injection.

Figure 3 shows the layout of the OMC testbed. The light starts at the OTA Simulator, which acts as the testbed's pseudo star, providing point source light with adjustable brightness and spectral bandwidth. It also creates the pupil with a shape that mimics the obscured 2.4-meter WFIRST telescope aperture. The OTA Simulator also creates and injects the expected on-orbit WFIRST wavefront drift and LoS error into the testbed. In the test we reported here the OTA Simulator was modified from previous OTA Simulator design, which we have temporarily removed the miniature telescope that used to collimate the light from pseudo star pinhole. Instead the light from pinhole is collimated by a long focal length (f = 60") off-axis parabola (OAP) mirror. So in this configuration we use the stage of source pinhole to create defocus as the way to inject the low order mode WFE. In the future, we plan to reinstall the miniature telescope back to OTA Simulator bench and use a pair of OAPs to form a reduced pseudo star before the telescope. This will help us to regain the capability of generating other low order WFE modes besides focus.

Efforts have been made to isolate the testbed from the environmental disturbances in the lab. The OMC testbed is operated inside a vacuum chamber. The vacuum chamber and optical bench are thermally controlled. Mechanically the OMC optical bench sits on three Minus-K isolators with rigid body mode of only 0.5 Hz. The recent upgrades of the testbed include improving the thermal control of the testbed optical bench, cameras, as well as the DMs. The temperature of DMs are now stable to a few mK. We have also replaced the JM and FSM cables with better shielding to reduce the electronic noise and cross talk. The testbed can be operated remotely and has a GUI for user to directly set up and change the hardware configurations on the testbed.

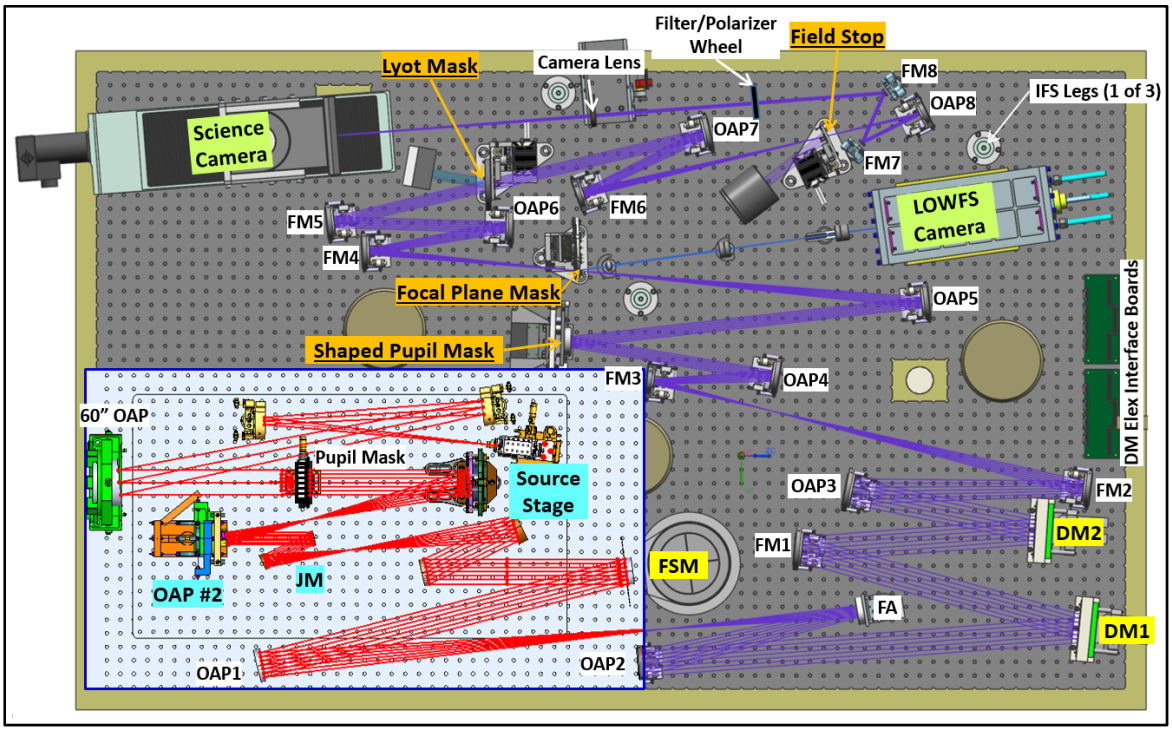

Figure 3. OMC testbed layout that shows the optical rays and opto-mechanical components on the optical table. The optical rays are from Zemax optical design. OTA Simulator is at lower left. Light from a fiber fed pinhole acts as the pseudo star is collimated by a 60" OAP and masked by a WFIRST pupil mask. Jitter Mirror (JM) is used to generate line-of-sight disturbances and pinhole source stage is used to generate focus as the disturbance of low order WFE. The output of the disturbed wavefront from OTA Simulator is coupled to the rest of coronagraph system at FSM, which is at one of the pupil planes. FSM, DM1 and DM2 are the active components on the testbed and they are used by HOWFS/C for starlight suppression and LOWFS/C for LoS and WFE disturbances suppression. Components with underlined labels are various coronagraph masks and stops for HLC and SPC. Off-axis parabola mirrors (OAP) and flat fold mirrors (FM) form various pupil and image planes for these masks and stops. Science Camera at upper left is used for star light suppression wavefront control (HOWFS/C) and coronagraph high contrast imaging. Rejected starlight from Focal Plane Mask (FPM) reflects to the LOWFS optics which form a properly sampled pupil image on the LOWFS Camera.

2 LOWFS/C PERFORMANCE UNDER FLIGHT LIKE PHOTON FLUX

2.1 Summery of previous dynamic tests

In our previous paper (SPIE 2017) [10, 11, 12] we have reported the testbed results from coronagraph and LOWFS/C dynamic tests in which we have demonstrated LOWFS/C can effectively suppress the WFIRST-like LoS and low order WFE disturbances and maintain coronagraph contrast to better than 10^{-8} for both SPC and HLC modes. During the dynamic test we injected three dominant disturbances modes expected for WFIRST flight: tip-tilt (slow drift and fast jitter) and focus. Figure 4 highlighted the HLC and SPC contrast with the LOWFS/C FSM and DM loops open and closed with the presence of WFIRST like disturbances. The LOWFS sensor has also demonstrated to have high sensitivity, capable of sensing LoS tilt to the level of 0.2 mas and low order mode to the level of 12 pm. We have also showed that residual errors from the line-of-sight control using the FSM and low order wavefront correction using a DM match the control models predictions very well.

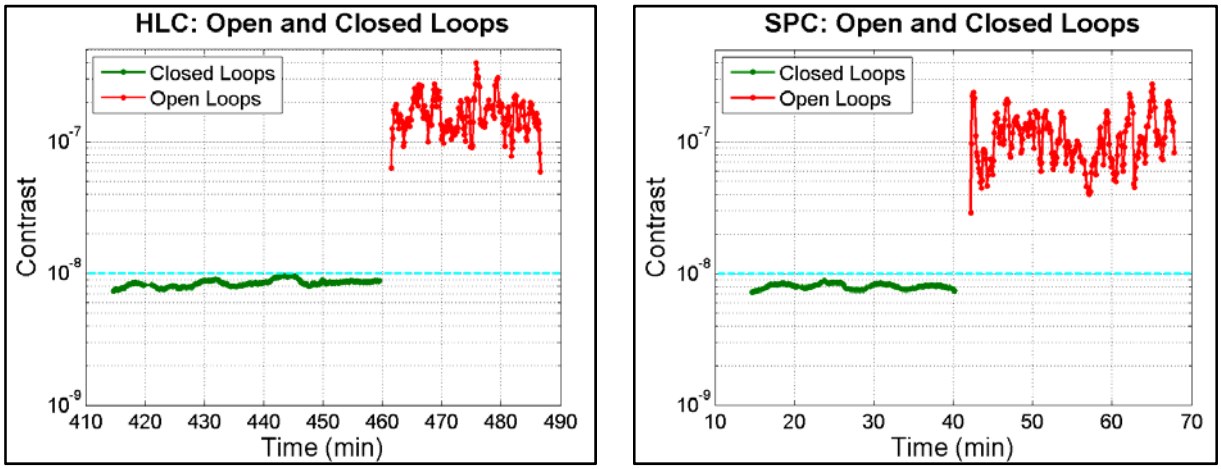

Figure 4. Summary plot of the dynamic test results reported in 2017 SPIE [10]. The plot on the left shows the HLC broadband contrast (10% centered at 550 nm) with LOWFS/C FSM and DM loops closed and open. The plots on the right shows that with SPC mode. During the tests the WFIRST like disturbances were injected using testbed's OTA Simulator. The disturbances include the LoS drift and jitter, which is corrected by LoS feedback and feed forward loops using FSM. The disturbances also include low order wavefront drift in the form of sinusoidal focus, which is corrected using one of the two DMs on the testbed. More details of the test setup can be found in our 2017 SPIE paper [10, 11, 12].

2.2 Test LOWFS/C with flight like photon flux

The dynamic tests reported in 2017 and summarized in Section 2.1 were done with a bright testbed source. The photometric calibration on the testbed has shown the source brightness used for these tests is equivalent to stellar magnitude of Mv = -3.5 for LOWFS camera when compared the per frame photon flux between the testbed and WFIRST flight. We need to evaluate the LOWFS/C performance under realistic photon flux expected during WFIRST flight and demonstrate that LOWFS/C can perform under low photon flux.

For WFIRST CGI LOWFS/C there are two types of stellar magnitude requirement from two CGI operation modes:

- The first mode is the CGI high contrast imaging initialization mode. In this mode the telescope will point to a bright reference star with stellar magnitude Mv = 2 or brighter. On the bright reference star CGI will perform high order wavefront control (HOWFS/C) to suppress the star light and create the high contrast imaging, or often referred as creating a "dark hole". During this period the LOWFS/C will also be turned on and simultaneously suppress any disturbances from the telescope such as LoS drift and jitter as well as thermally induced low order wavefront drift. Since HOWFS/C uses both DMs and LOWFS/C uses one of the DMs for low order wavefront control the LOWFS/C control target is slaved to HOWFS/C so both loops can work cohesively together [13]. In this CGI initialization mode the LOWFS sensor need to work with reference star of brightness Mv ≤ 2.
- The second mode is the CGI observation mode. This mode follows the CGI high contrast imaging initialization mode. In this mode, with the CGI dark hole established, the telescope will point to a science target with stellar magnitude about Mv = 5. During science target observation the science camera will not be used for starlight suppression wavefront control (HOWFS/C). Instead the science camera will be used to carry long exposures for planet light observation. However, the LOWFS/C will continue be turned on to suppress the wavefront disturbances in order to maintain the coronagraph contrast needed for coronagraphic observation. The LOWFS/C needs to perform with science target star of brightness Mv ≤ 5.

To test LOWFS/C for low flux we first need to photometrically match the photon flux on the testbed LOWFS camera to that of WFIRST CGI LOWFS camera. Although the optical transmission for LOWFS path is about the same for the testbed and flight instrument (both T ~ 0.26 for HLC) there are many differences between the testbed and the flight instrument, such as LOWFS camera frame rate (testbed: 500 Hz, flight:1000 Hz), LOWFS camera exposure time (testbed: 0.3 music, flight: 1 music), source spectral (testbed: super continuum laser, flight: real star spectrum), source bandwidth (testbed: 100 nm for HOWFS/C and 55 nm for contrast observation, flight: 128 nm base line design), readout noise (testbed: ~2e, flight: ~5e), detector quantum efficiency (QE) (testbed: 0.6, flight: 0.9), and camera

conversion gains (DN/photon electron). However, by realizing that the LOWFS sensor performance is dominated by the photon noise for fainter star we decide to match the LOWFS camera total photon electrons per frame to that of the flight camera so that for any given stellar magnitude the total photon electrons in each frame is the same for testbed and flight. Using total photon electrons per frame has captured the net effect of camera exposure time, QE, and source bandwidth and equalized the fundamental sensor noise source. The stellar flux for flight is based on a G0V star's UBVRI photometry [14] which at Mv = 0 has 1.3×10^{10} photons/m^2/sec over the 128 nm (centered at 550 nm) bandwidth the flight LOWFS camera is designed for. The WFIRST telescope has a total collecting area about 3.6 m^2 and LOWFS optical transmission is about 0.26 for HLC and 0.1 for SPC. The testbed source is a commercial super continuum laser source. The source bandwidth is usually set to be 100 nm (18%) centered at 550 nm during HOWFS/C control to create dark hole. HOWFS/C uses a set of narrow band filters in front of science camera. When we do the broad band contrast measurement we usually set the source bandwidth to 55 nm (10%). Since the LOWFS camera frame rate, exposure and source bandwidth are fixed in order to change the photon flux on LOWFS camera to the equivalent stellar magnitude we used a step variable neutral density (ND) filter. The step variable ND filter is on a motorized stage mounted in front of the LOWFS camera. We also used the super continuum laser power setting to change the photon flux on the LOWFS camera in finer scale.

Figure 5 shows the example of single frame image from testbed LOWFS camera under different stellar magnitude. It shows that as the source getting fainter the LOWFS image has less DN counts and photon noise is more pronounced.

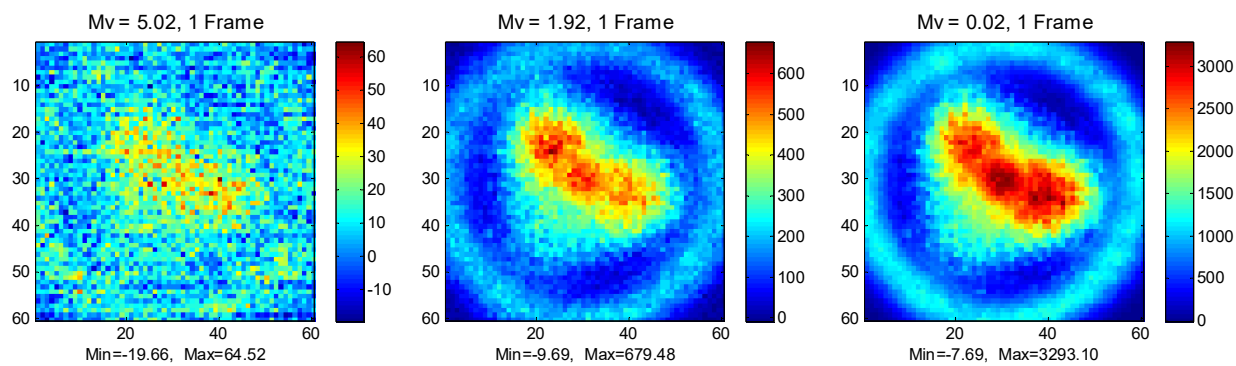

Figure 5. LOWFS camera single frame image under different equivalent stellar magnitude. The images are dark removed and in unit of camera DN. The color bar on the right of each image shows the intensity range and X-label shows the minimum and maximum pixel value of the image. The morphology of the LOWFS image is the result from the HOWFS/C DM setting. From left to right the equivalent stellar magnitude are Mv = 5, Mv = 2, and Mv = 0.

In following sections we will present the testbed results on LOWFS/C performance under low photon flux, especially the LOWFS/C performance with stellar magnitude of $M \leq 5$ which is required in the science target observation mode. We should point out that on the testbed we have also demonstrated the simultaneous starlight light suppression wavefront control (HOWFS/C) and LOWFS/C correcting the injected WFIRST like line-of-sight and wavefront (focus) disturbances on an Mv = 2 star, simulating the coronagraph high contrast initialization mode. The detail on this test will be discussed in our companion paper in this SPIE [13].

2.3 LOWFS sensor noise vs. photon flux

Compared to the flight required stellar magnitude (Mv ≤ 2 for initialization mode or Mv ≤ 5 observation mode) the LOWFS camera photon flux used for the previous testbed dynamic test is 2 or 3 order magnitude brighter (Mv = -3.5). We have carried out several test to evaluate the LOWFS performance under low photon flux.

To understand the LOWFS sensor performance under various photon flux level we measured the LoS error under different photon flux conditions with the testbed in a quiet lab environment and FSM loop closed. The measured rms LoS errors against the equivalent stellar magnitudes are plotted in logarithmic scale in Figure 6. The red and blue curve in Figure 6 shows the modeled testbed LOWFS LoS sensor noise against equivalent stellar magnitude. The model uses the modeled LOWFS image morphology and contains photon noise. It uses the testbed camera parameter,

such read out noise (RON) and pupil sampling. The model only considers sensor noise from the photon noise, detector read out noise, and dark current. The rms sensor noise in the plot are resulted from Mote Carlo exercise of model. The sensor noise curves shows that for bright stars (Mv ≤ 5) the sensor noise is dominated by photon noise, indicated by the linear relationship between the sensor noise and stellar magnitude. At the fainter stellar magnitude end (Mv > 5) the contribution from detector's RON becomes more significant, causing the curve to deviate from linear relationship and rise up faster with the stellar magnitude. Comparing testbed data and modeled curve we notice that the testbed data agree well with the modeled sensor noise at fainter stellar magnitude, indicating under the low flux most of sensor noise for both testbed and model are dominated by the photon noise and detector RON. As the photon flux increases (from right to left) the sensing error reduces but the testbed data levels off around 0.2 mas after Mv ≤ 4. This is because the testbed data contains not only the sensor noise but also the lab environment jitter that FSM loops cannot correct. Those jitters are from high frequencies vibrations from motors on the testbed as well as the electronic noise on FSM and JM actuators. The PSD and frequency integrated LoS error in Figure 8 show the jitter noise from the lab environment.

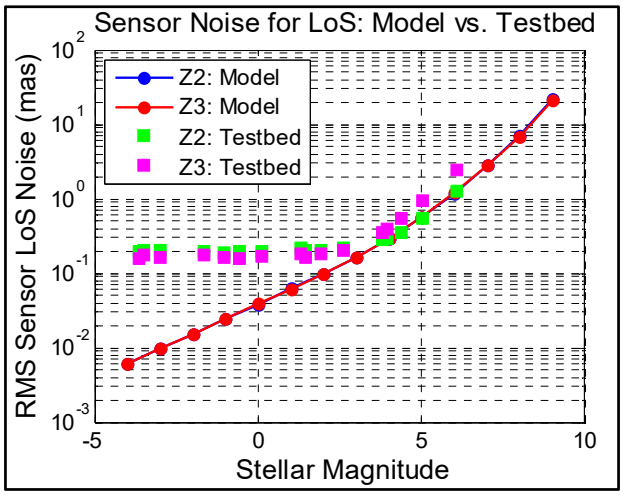

Figure 6. Comparing LOWFS testbed LoS error measured under quiet lab environment with modeled LOWFS sensor noise against photon flux. The LoS error has been converted to on-sky LoS angle (milli-arcsecond) (Y-axis) and photon flux has been converted to stellar magnitude (X-axis). The testbed data contain lab environment jitter so they remain constant when the source is brighter than Mv ≤ 4. Under a bright source the testbed measured Z2 is lightly larger than Z3 because the there is more out of plane tilt (Z2) jitter than Z3. However, under a faint source the Z3 is bigger than Z2 because the testbed LOWFS camera is a CMOS camera which suffers asymmetric sensor noise between the camera rows and columns.

2.4 LOWFS/C ling-of-sight loop performance under low photon flux

One of the test to evaluate the LOWFS sensor performance under low flux we have done is to see LOWFS measurement response to a fix tilt input. We used the FSM actuator chopping at a fix input command as constant tilt input and examine the sensor measurement of the chopping amplitude under various photon flux levels. Using chopping amplitude for sensor measurement eliminates the effect of the long term testbed drift. Each FSM actuator has a local strain gauge loop to ensure its motion is linear and repeatable. The FSM tilt has been calibrated by Zygo externally and again by science camera for its tilt plate scale after the recent cable replacement. The top plot in Figure 7 shows the measured Z2 and Z3 tilt chopping amplitude against the equivalent stellar magnitude. The chopping signal of ±1V is applied to one of the FSM actuators (Ch3) and because of the triangular location the FSM actuators the Ch3 actuator motion generates tilt in both Z2 and Z3. The bottom plots show example of the LOWFS raw measurement at stellar magnitude of Mv = -3.5, Mv = 2.0, and Mv = 5.0. The amplitude of chopping is the averaged difference between the positive and negative chopping signals. The top plot of Figure 7 shows that the sensors measurement of the chopping amplitude is fair constant throughout a very large photon flux variation, from Mv = -3.6 to Mv = 6, which is almost 4 order of magnitude. This has validated the sensor measurement performance for different photon flux levels.

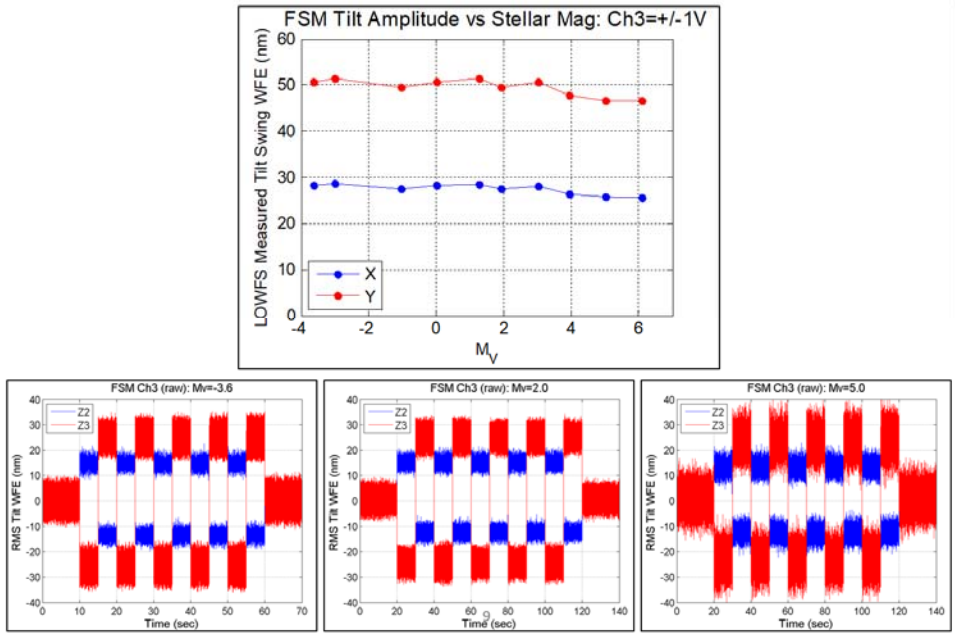

Figure 7. Top plot the testbed LOWFS tilt amplitude measurement vs. stellar magnitude. The bottom plots are the LOWFS raw signals measurement time traces responding to the FSM Ch3 chopping under photon flux of Mv = -3.6 (left), Mv = 2.0 (middle), and Mv = 5.0 (right). The LOWFS measurement frequency is 500 Hz. The chopping signal starts with 0V on FSM Ch3, then follows with 5 cycles of ±1V chopping and then comes back to 0V. The LOWFS tilts (Z2 and Z3) measurements are in unit of nm (RMS). The plot on the top is the averaged chopping amplitude between positive and negative chops. Noticed that while the raw signals from Mv = 5.0 is significantly noisier (bigger "fuzz") due to the low photon flux. The raw signals of Mv = -3.6 and Mv = 2.0, however, have the similar noise level ("fuzz"). This is because as shown in Figure 6 the sensor noise for bright sources are limited by the lab environment jitter.

Figure 8 shows the LOWFS line-of-fight open and closed loop performances from the dynamic test under stellar magnitude of Mv = 2.5 and Mv = 5.0. The plots show the LOWFS tilt measurement PSD and forward integrated tilt error. During the test the WFIRST like LoS disturbances are injected into the testbed using the testbed OTA Simulator's Jitter Mirror (JM). The disturbances include WFIRST altitude control system (ACS) residual LoS drift (frequency ≤ 1 Hz) and LoS jitter induced by the WFIRST reaction wheel assembly (RWA) at speed of 600 rpm (10 Hz), which is the worst case wheel speed. The RWA induced jitter includes jitter at fundamental frequency (10 Hz), which is dominant, and jitter at other 72 harmonic frequencies. The LoS disturbances amplitude comes from the observatory integrated modeling. The testbed open loop PSD also show some lab environment jitters (120 Hz, 145 Hz, etc), not related to the WFIRST. As discussed in Section 1.2 the LoS control loops consists of feedback loop which has closed loop bandwidth about 10 Hz and feedforward loop which forms notches at fundamental and sub-harmonic frequencies of RWA jitters. To reduce the lab environment jitters we also put two more notches for the 120 Hz and 145 Hz. The plots in Figure 8 shows that the LoS closed loops work well under both Mv = 2.5 and Mv = 5.0 source. The residual error for Mv = 2.5 is mostly high frequency lab environment jitter which are beyond the FSM control. Under both stellar magnitude the closed feedback loop bandwidth and feed forward loop notches have effectively suppressed the injected LoS drift and jitter. The effectiveness of LOWFS/C disturbances suppression is reflected from the measured coronagraph contrast recorded at the same time with the LOWFS/C loops open and closed (Figure 9 and 10). Comparing the closed loop LoS residual between Mv = 2.5 and Mv = 5.0 we noticed that the results from fainter source have more broad band noise residual error. This is caused by the noisier sensor measurement for the faint star and does not reflect the true wavefront tilt error on the testbed because the control loop has been shaped to reduce the noise impact on the loop. The true residual tilt error can be measured by the coronagraph contrast (Figure 9) which is the ultimate goal of the loops the LOWFS/C is designed for.

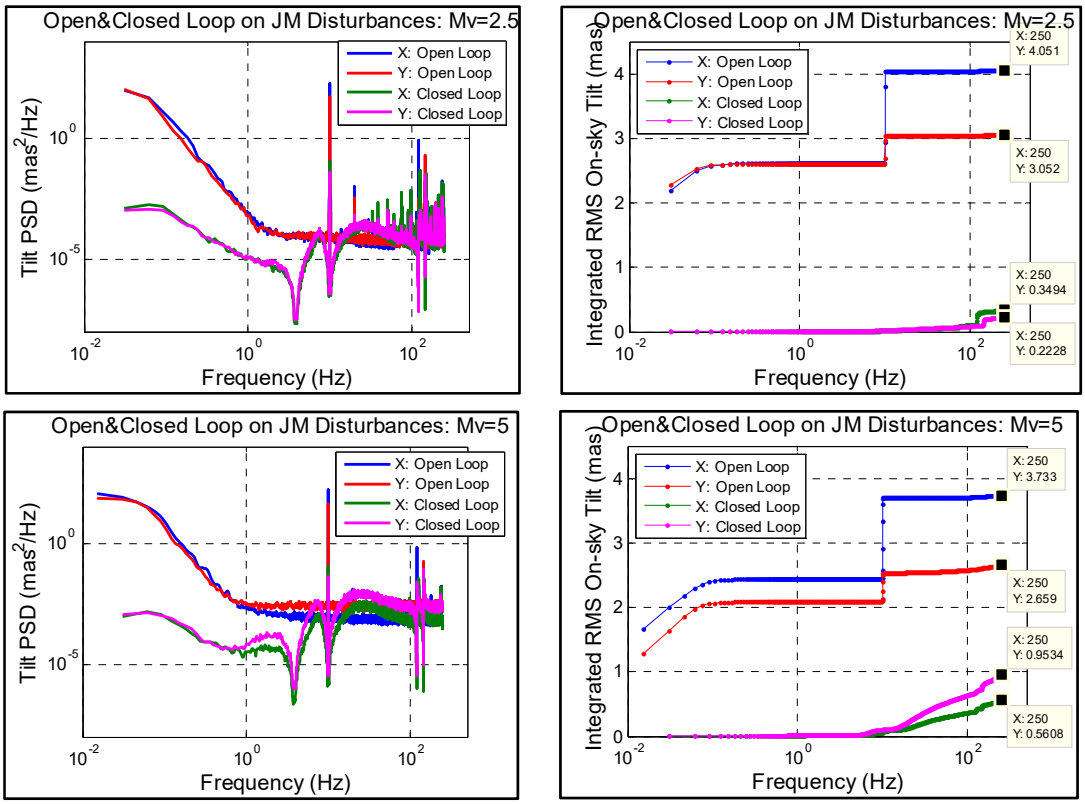

Figure 8. LOWFS/C sensed open and closed loop tilts PSD (left) and forward frequency integrated accumulation of tilts (right). The top two plots are from a source brightness of Mv = 2.5 and bottom two plots are from a fainter source of Mv = 5.0. As indicated in the legend the open loop X and Y tilts are plotted in blue and red while the closed loop X and Y tilts are in green and pink. The Y values of data cursor at the end of forward integrated accumulation curves show the total tilt errors (X = 250 Hz is the Nyquis frequency of camera running at 500 Hz.) All tilt errors in the plot have been converted to on-sky LoS tilt in unit of mas.

Figure 9 shows the HLC contrast from the dynamic tests with LOWFS/C LoS loops for a faint source (Mv = 5). At beginning of the dynamic test the coronagraph star light suppression wavefront control (HOWFS/C) has established a good dark hole (broadband contrast ~6×10^{-9}) and HOWFS/C is then stopped. During the dynamic test the coronagraph science camera is only taking the broadband contrast measurement (10% bandwidth centered at 550 nm over 3–9 λ/D) continuously providing a broadband contrast measurement every 25 sec. Also while the LOWFS camera was under the low photon flux from the ND filters in front of the LOWFS/C camera the coronagraph contrast monitoring was done with a high photon flux for a good signal-to-noise (SNR) contrast measurement. During the dynamic test we took data with FSM loops turned on and off as well as with LoS disturbances turned on and off. The detail conditions corresponding to the HLC contrast plot are listed in the figure captions in Figure 9. From the plot in Figure 9 we can see in the section B with the WFIRST like LoS disturbances injected and LOWFS/C LoS closed loop control is able to maintain the HLC contrast to around 6.5×10^{-9}, well below the intended target of 10^{-8}. Compared to the coronagraph contrast in section D when the LOWFS/C LoS control is turned off the HLC contrast has been greatly degraded by the disturbances, to a level of a few times 10^{-7}. The effectiveness and importance of LOWFS/C working under low photon flux are validated from the open and closed loops contrast differences between sections D and B in the plot, demonstrating the LOWFS/C performance in the scenario of the coronagraph science target observation.

For the same dynamic test sequence we have repeated with different photon flux levels. Figure 10 shows the HLC broadband contrast using source brightness of Mv = 5.0 (same as Figure 9), Mv = 0.0 and Mv = 2.5. The plot shows the under different source brightness the LOWFS/C has the similar contrast results. For three cases the LoS close loops are able to maintain the contrast with the presence of WFIRST like LoS disturbances. This is yet another

indication of LOWF/C perform well across all stellar brightness, consistent with the sensor chopping test shown in Figure 7.

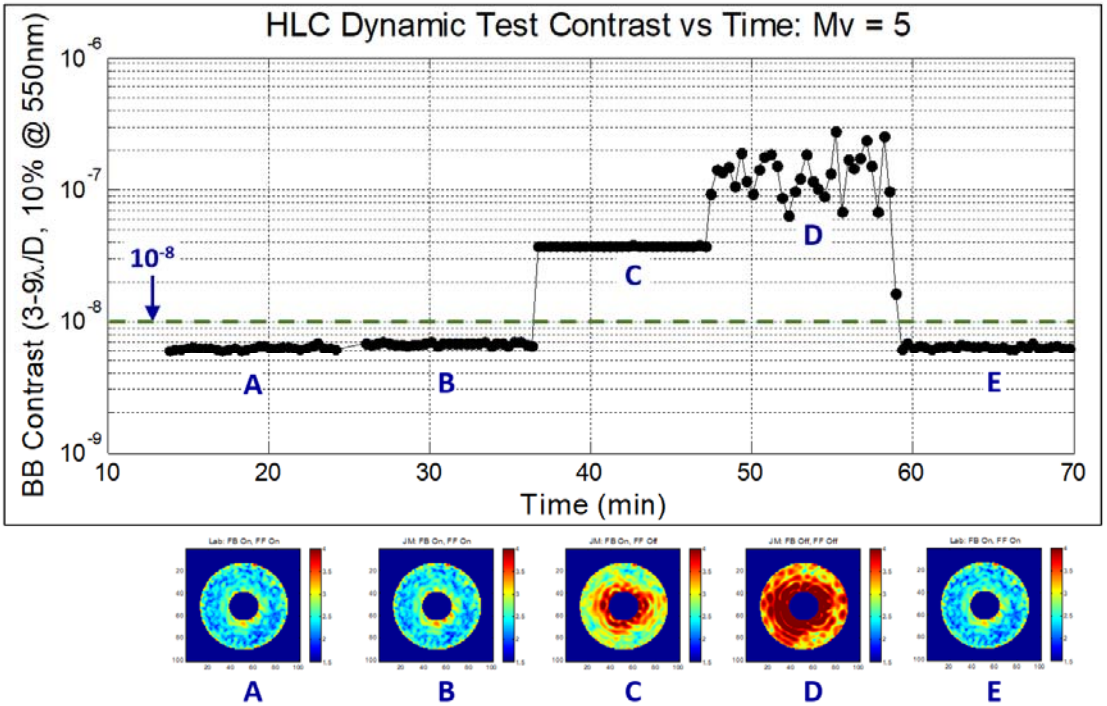

Figure 9. Testbed HLC broadband contrast recorded during the dynamic test on a source with brightness equivalent to an Mv = 5 star. There are 5 segments of tests labeled **A** to **E**, each about 10 minutes long. The plot follows the actual test time sequence. The disturbances and LoS loops conditions are: **A**: LoS feedback and feed forward loops turned on under the lab environment; **B**: LoS feedback and feed forward loops turned on with the JM induced WFIRST like dynamics disturbances (ACS drift + jitter from RWA at 600rpm); **C**: LoS feedback loop turned on but feedforward loop turned off with the JM induced WFIRST like dynamics disturbances (ACS drift + jitter from RWA at 600rpm); **D**: both LoS loops turned off with the JM induced WFIRST like dynamics disturbances (ACS drift + jitter from RWA at 600rpm); **E**: Turned off JM disturbances. LoS feedback and feed forward loops turned back on under the lab environment. This segment (**E**) is the same as segment **A** and provide the monitor of the long term testbed drift. Plotted under the contrast plot are the example HLC high contrast images from each segment. They are displayed in the same logarithmic stretch for easy comparison. These images show the impact of disturbances and loops to the dark hole.

It is of great interest to take a closer look at the contrast level difference between segment **A** and segment **B** of plots in Figure 9 and 10. Both segment **A** and **B** show the LOWFS/C LoS control loops performance. However, in segment **A** the JM disturbances is turned off and testbed is only under the much quieter lab environment (from Figure 6 the lab residual jitter is ~0.2 mas) while in segment **B** in addition to the lab environment the JM on the testbed has also injected WFIRST like LoS disturbances (~4 mas as shown in Figure 8) into the testbed. Even with the FSM loops closed there still some LoS residual from WFIRST LoS disturbance so that the contrast level of segment **B** will be worse than that of segment **A**. This is shown in Figure 11 which is the zoomed in view of **A** and **B** segment from the plot shown in Figure 9. The mean contrast within the **B** segment in which the WFIRST LoS disturbances have been turned on is slightly but visibly higher than the mean contrast in segment **A** which only suffered quiet lab environment. The left plot of Figure 12 shows the plot of the mean contrast difference $\Delta C(M_V)$ between segment **B** and **A** under different source brightness (Figure 10) against stellar magnitude Mv. The mean contrast difference can be expressed as,

$$\Delta C(M_V) = \overline{C_B(M_V)} - \overline{C_A(M_V)} = \overline{C_{JM}(M_V)} - \overline{C_{Lab}(M_V)} \quad (1)$$

We use the subscript *JM* to indicate the testbed condition of segment **B** is with JM injecting the WFIRST LoS disturbances and subscript *Lab* to indicate the segment **A** is under quiet lab environment. The left plot in Figure 12 has shown that the delta contrast depends on the source brightness. The brighter source has smaller delta contrast, indicating better LoS control due to the less sensor noise. In principle the coronagraph contrast goes with the power of residual wavefront error so the difference of contrast level between segment **B** and **A** is a direct measurement of LOWFS/C LoS control residual tilt errors on the WFIRST like LoS disturbances. To convert the delta contrast to the tilt errors we need the contrast-to-tilt sensitivity. The testbed measured contrast-to-tilt sensitivity is $1.9x10^{-9}\ \Delta C / mas^2$ *per axis* [3]. Here the ΔC is the change of broadband (10% centered at 550 nm) contrast measured over 3 – 9 λ/D. Assuming the residual tilt errors are uniformly distributed between X and Y axes from the ΔC of the left plot in Figure 12 and contrast-to-tilt sensitivity we can calculate the post correct residual tilt error from the LOWFS/C LoS correcting the WFIRST disturbances. The residual tilt errors for suppression of WFIRST LoS disturbances against the stellar magnitude is plotted on the right in Figure 12. From this plot we can see that at Mv = 5 the residual tilt is about 0.36 mas, well under the 0.5 mas requirement from WFIRST CGI error budget [3].

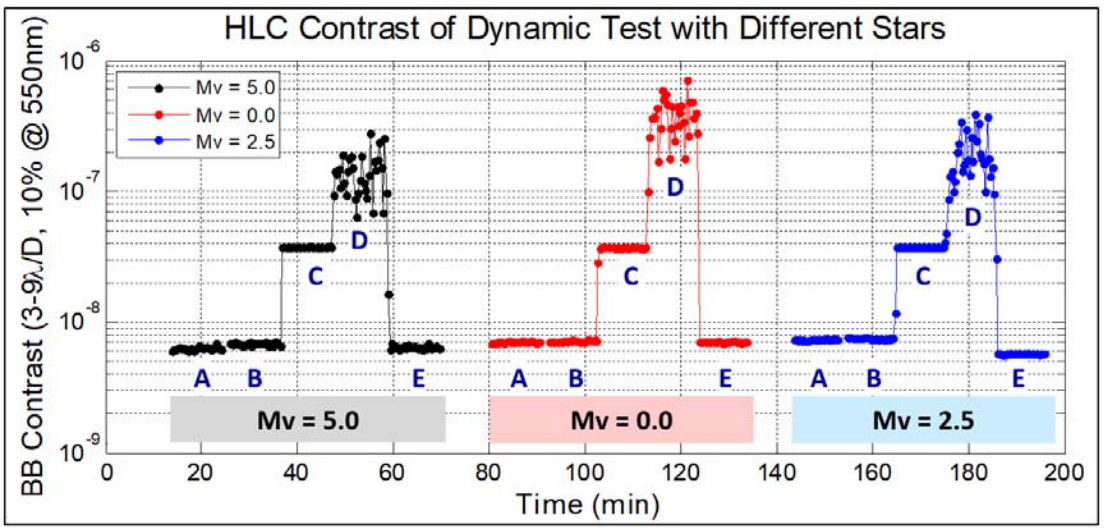

Figure 10. Testbed HLC broadband contrast recorded during the dynamic test on different source brightness. The source brightness are equivalent to Mv = 5 (in black), Mv = 0.0 (in red), and Mv = 2.5 (in blue). The HLC contrast time plot follows the actual sequence of our test. For each source brightness there are 5 segments of test labeled **A** to **E**, each about 10 minutes long. The disturbances and LoS loops conditions are: **A**: LoS feedback and feed forward loops turned on under lab environment; **B**: LoS feedback and feed forward loops turned on with JM induced WFIRST like dynamics disturbances (ACS drift + jitter from RWA at 600rpm); **C**: LoS feedback loop turned on but feedforward loop turned off with JM induced WFIRST like dynamics disturbances (ACS drift + jitter from RWA at 600rpm); **D**: LoS both loops turned off with JM induced WFIRST like dynamics disturbances (ACS drift + jitter from RWA at 600rpm); **E**: Turned off JM disturbances. LoS feedback and feed forward loops turned on under lab environment. This segment (**E**) is the same as segment **A** and provide the monitor of the long term testbed drift.

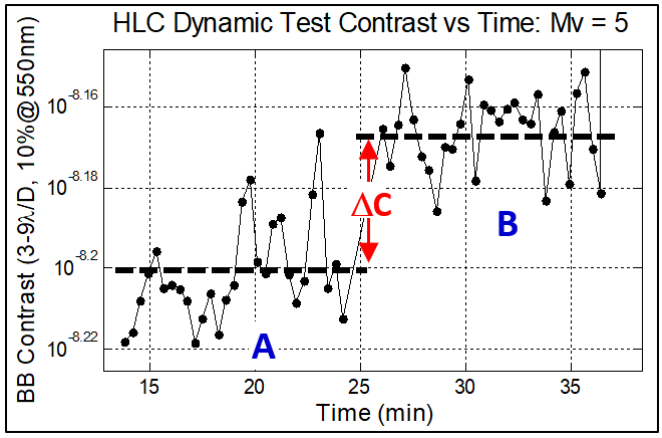

Figure 11. Zoomed in plot of HLC broadband contrast showing contrast in segment **A** and **B** (from Figure 9) for the test using source brightness of Mv = 5. The plot shows that contrast of **B** segment as whole is visibly higher than that of **A** segment. The **B** segment is with WFIRST disturbances injected by JM while segment **A** is with the testbed under quiet lab environment. The mean of each segment, which is indicated by the black dash lines, are used to calculate the delta contrast, indicated in red, $\Delta C(M_V)$ for the corresponding Mv.

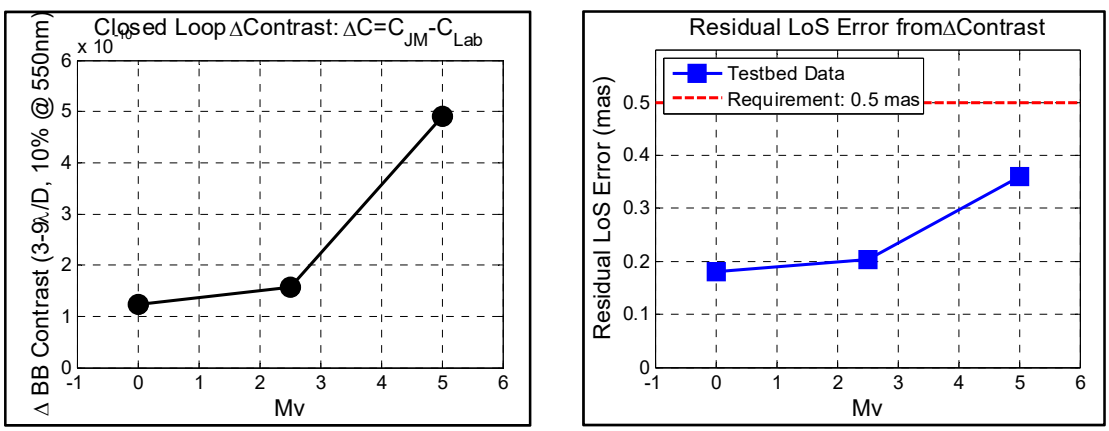

Figure 12. Left: Testbed measured delta contrast (Eq 1) vs. stellar magnitude. The delta contrast is the mean contrast difference between the LoS disturbance injected case (**B**) and lab quiet environment case (**A**), both with the LOWFS/C LoS loops closed. Right: LOWFS/C LoS loops post correction residual tilt error calculated from the delta contrast shown on the left using the testbed measured contrast-to-tilt sensitivity. The post correction LoS error requirement (0.5 mas) is indicated by the red dash line.

2.5 LOWFS/C DM loop performance under low photon flux

Similar to the test shown in Figure 7 we tested LOWFS sensor measurement response to a fixed low order wavefront error under various photon flux levels. We used the testbed OTA Simulator's pseudo star pinhole source stage to generate a sinusoidal focus modulation as the know input of low order WFE. The source stage has an accuracy of 1 um and motion to wavefront scale is 32 um stage motion corresponding to 1 nm wavefront focus. The plots in Figure 13 shows a few examples of the LOWFS measurement to a fix amplitude sinusoidal wavefront focus input under different source brightness (Mv = -1.0, Mv = 2.6, Mv = 4.7). The plots in Figure 13 show that at 500 Hz the raw sensor

measurement become much noisier as the source getting fainter. However, a simple 5-second box car average removes most of sensor noise. Also the fitted sine wave amplitude (with or without the 5-sec averaging) remains fairly contestant for the different source brightness. For WFIRST the thermally induced low order wavefront drift is very slow (~0.001 Hz) which allows LOWFS sensor to use long average to reduce the sensor noise. During the test we used the 5-sec averaged sensor data to drive the DM low order control loops for the low order WFE (focus) correction.

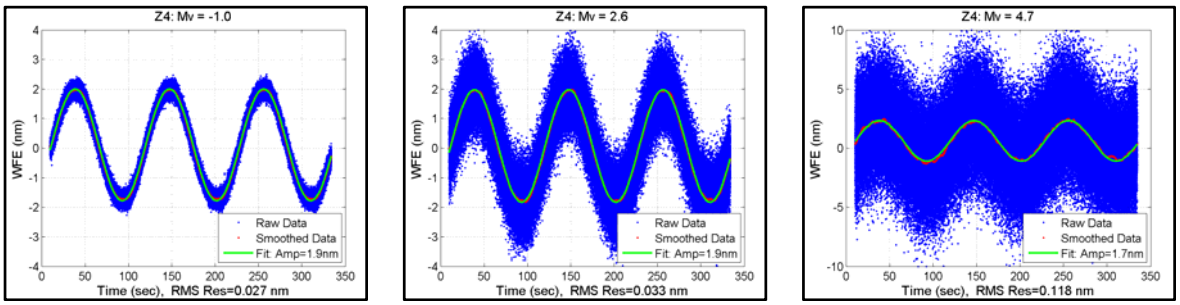

Figure 13. Example of LOWFS measurement to a fixed amplitude sinusoidal focus error input. The raw sensor measurement comes at 500 Hz is plotted in blue dots. The 5 sec averaged data is in red. The sinusoidal fit is in green and it is used to compare LOWFS sensor measurement under different source brightness.

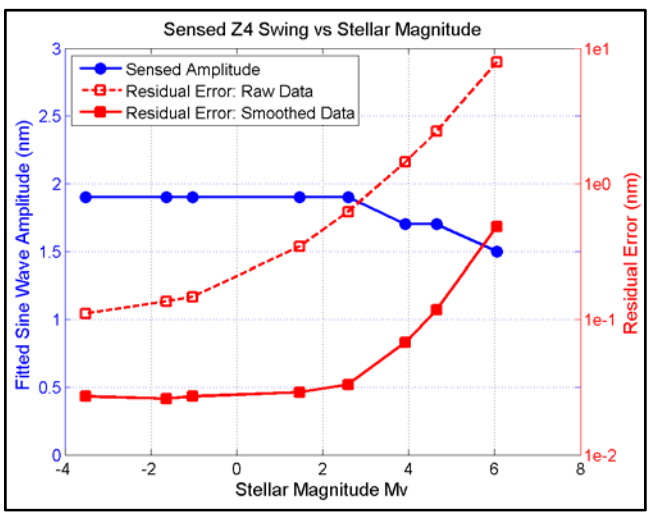

Figure 14. Testbed LOWFS sensor low order WFE (focus) measurement under various source brightness. The X-axis is equivalent source magnitude. The plot has two Y-axes. The left Y-axis is for the sensed sine wave amplitude (blue curve) vs stellar magnitude. The right Y-axis is for the residual errors after the fitted sine wave is removed from the raw (red curve with open squares) and 5-sec averaged (red curve with filled squares) measurements against Mv. Please note that residual errors are plotted in logarithmic scale.

Because the input focus sine wave input is fixed we use the fitted sine wave amplitude and residual after the fit to compare the LOWFS sensor performance on focus (Z4) measurement. Figure 14 shows the LOWFS measured sine wave amplitude against equivalent stellar magnitude (blue curve read on the left Y-axis) as well as the corresponding residual errors after the fitted sine wave is removed from the raw and 5-sec averaged measurement (red curves read on the right Y-axis). From the plots we can see that the measured sine wave amplitude remains fairly constant across different stellar brightness. However, there is a little drop on the amplitude for the fainter stars, at Mv = 5 the difference is 10% lower than the measurement under bright source. The residual error plots in Figure 14 show that the sensor

error is dominated by the photon noise at the faint source end because the sensing error increases with the stellar magnitude and follows a power law (straight line). A 5-sec averaging has significantly reduced the residual sensing error. The plot has also indicated the sensing error can still be further improved with longer average. At bright source end the 5-sec averaged residual error flatten off to 0.026 nm after the source brighter than Mv = 2. We believe this is caused by source stage actuator backlash which caused the motion of source not quite pure sinusoidal. This effect is visible from the plots in Figure 13 which show the 5-sec averaged curve (red) deviating the sine wave fit (green) at top and bottom of the sine wave, where the stage backlash is the strongest. Nevertheless a residual sensing error of 26 pm is still a good performance of sensor and has little impact on contrast. The plots in Figure 14 show the LOWFS/C low order WFE sensing has performed very well across the source brightness varying over 4 orders of magnitude.

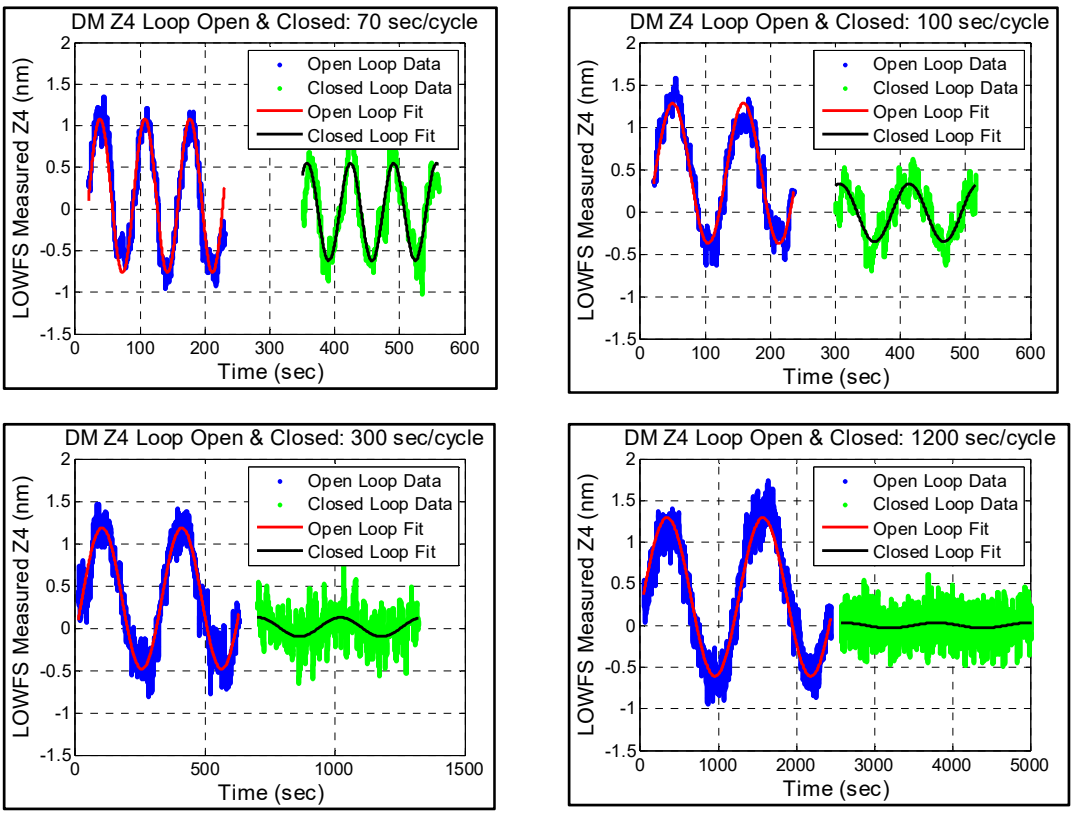

Figure 15. Testbed low photon flux (Mv = 5) focus (Z4) measurement from open and closed DM low order WFE correction loop. The four time trace plots show test results with different focus sine wave frequencies. The frequencies from high to low are: upper left: 0.01428 Hz (70 sec/cycle), upper right: 0.01 Hz (100 sec/cycle), lower left: 0.0033 Hz (300 sec/cycle), and lower right: 0.0008 Hz (1200 sec /cycle). In each plot the time trace starts with open loop data and then follows with closed loop data. The testbed data is 5-sec averaged and fitted by sinusoidal signal as a measure of the focus swing.

The plots in Figure 15 shows the testbed results of LOWFS/C low order WFE control using a DM under the fain source (Mv = 5). In this test we used the source stage to generate sinusoidal focus error with amplitude of ~1 nm with different frequencies. The focus sine wave cycle frequencies range from 70 sec/cycle (frequency = 1/70 s = 0.0143 Hz) to 1200 sec/cycle (frequency = 1/1200 s = 0.0008 Hz). At each frequency we started with the DM loop open for a few cycles of focus swing and then closed the DM loop for another few cycles of focus change. The LOWFS/C DM control loop is a simple integral feedback control using the 5-sec averaged LOWFS sensor data as the input. The 5-sec average is empirically set based on our analysis of the raw data. The LOWFS/C low order WFE DM loop has a 0 dB bandwidth of 0.02 Hz. During this test we only use the DM to correct the focus (Z4) mode. Figure 15 shows some of the open and closed loop senor measured focus (Z4) at different focus swing frequencies in this test. From the plot we can see that the LOWFS/C DM loop performs well under the low photon flux. As expected, the post DM loop

correction residual depended on the input sine wave frequency. The ratio of the fitted residual and input amplitude, which is a measurement of error transfer function (ETF), is plotted in Figure 16 and compared with the model predicted ETF. The Z4 control model uses the testbed condition of 5-sec sensor average, 3 sec DM actuator application delay and gain of 0.5. The plots in Figure 16 show that the testbed measured DM loop focus rejection match very well with the model prediction. The testbed results in Figure 15 and 16 have showcased the good performance of low flux LOWFS/C low order WFE correction using a DM.

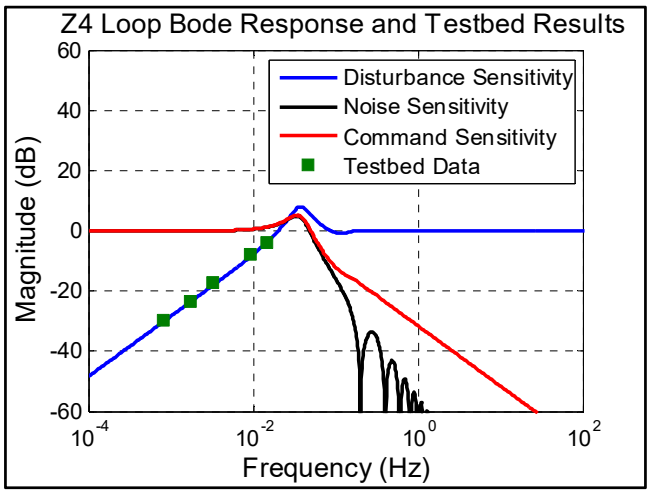

Figure 16. Testbed DM focus correction closed-loop error transfer function (ETF). The blue line is the DM control model predicted ETF and the green dots are the testbed LOWFS data from calculated from the results in Figure 15.

3 CONCLUSION AND FUTURE WORK

After a successful dynamic tests that have demonstrated the LOWFS/C can maintain the coronagraph contrast to better than 10^{-8}, we continue the LOWFS/C test which have concentrated on the LOWFS/C performance under the realistic WFIRST CGI flight like photon flux. Testbed results have shown that for a fixed low order wavefront error (tip, tilt and focus) the LOWFS measurement remain to be constant throughout a source brightness that varies almost 4 order of magnitude (~10,000X) to equivalent stellar magnitude as faint as Mv ~ 6. With WFIRST like line-of-sight jitter disturbances injected by the testbed OTA Simulator's Jitter Mirror the LOWFS/C LoS FSM loops have demonstrated to be able to maintain the contrast stability well under 10^{-8} for source as faint as Mv = 5. The post correction residual jitter, measured by broadband coronagraph contrast, has shown to meet the WFIRST jitter requirement of 0.5 mas. The LOWFS/C low order WFE DM loop performed well to source as faint as Mv = 5 and the testbed measured focus error transfer function matches the model prediction very well. Although not discussed in detail we have also demonstrated simultaneous starlight light suppression wavefront control (HOWFS/C) while LOWFS/C is correcting the injected WFIRST like line-of-sight and wavefront (focus) disturbances on a Mv = 2 star and more detailed discussion on this dynamic test can be found in the companion paper in this SPIE [13].

Coronagraph and LOWFS/C technology developments continue on the OMC testbed. For low flux LOWFS/C test we will continue to understand and improve the LOWFS/C DM loops post correction residuals. We will integrate an existing integral field spectrograph (IFS) onto the OMC testbed to demonstrate CGI spectroscopy mode working with LOWFS/C under dynamic conditions. We also plan to update the OTA-Simulator with a new jitter mirror and pinhole relay optics which will provide more capabilities of dynamic wavefront test. With testbed being improved and evolved, we will further improve the coronagraph performance, algorithm robustness, calibration accuracy, control efficiency, and model agreement. Eventually we will transform the technology development testbed into a WFIRST CGI instrument engineering testbed to test CGI flight hardware and algorithms, and more importantly, support the WFIRST CGI flight instrument I&T.

ACKNOWLEDGMENTS

This research was carried out at the Jet Propulsion Laboratory, California Institute of Technology, under a contract with the National Aeronautics and Space Administration. The work published in this paper was funded by NASA's WFIRST project. The decision to implement the WFIRST mission will not be finalized until NASA's completion of the National Environmental Policy Act (NEPA) process. This document is being made available for information purposes only.

REFERENCES

[1] Krist, J., Nemati, B., and Mennesson, B., "Numerical modelling of the proposed WFIRST-AFTA coronagraphs and their predicted performances," JATIS **2**, (2016).

[2] Krist, J., Riggs, A.J., McGuire, I., Tang, H., Amiri, N., Gutt, G., Marchen, L., Marx, D., Nemati, B., Saini, N., Sidick, E., Zhou, H., "WFIRST coronagraph optical modeling," Proc. SPIE **10400**, 10400-04, (2017).

[3] Poberezhskiy, I, Kern, B., et al, "WFIRST CGI: performance predictions for an active space coronagraph," Proc. SPIE **10698**, 10698-244, (2018)

[4] Krist, I., "WFIRST coronagraph flight performance modeling," Proc. SPIE **10698**, 10698-90 (2018)

[5] Shi, F., Balasubramanian, K., Hein, R., Lam, R., Moore, D., Moore, J., Patterson, K., Poberezhskiy, I., Shields, J., Sidick, E., Tang, H., Truong, T., Wallace, J. K., Wang, X., and Wilson, D., "Low Order Wavefront Sensing and Control for WFIRST-AFTA Coronagraph," JATIS **2**, (2016).

[6] Balasubramanian, K., White, V., Yee, K., Echternach, P., Muller, R., Dickie, M., Cady, E., Ryan, D., Poberezhskiy, I., Zhao, H., Kern, B., Krist, J., Nemati, B., Patterson, K., Riggs, A.J., Zimmerman, N., and N. J. Kasdin, "WFIRST-AFTA coronagraph shaped pupil masks: Design, Fabrication and Characterization," JATIS **2**, (2016).

[7] Balasubramanian, K., Riggs, A. J., Cady, E., White, V., Yee, K., Wilson, D., Echternarch, P., Muller, R., Prada, C. M., Seo, J., Shi, F., Ryan, D., Fregoso, S., Metzman, J., Wilson, R. C., "Fabrication of WFIRST coronagraph masks and laboratory scale star-shade masks: characteristics, defects, and performance," Proc. SPIE **10400**, 10400-12, (2017).

[8] Shields, J., Shi, F., Lam, R., Truong, T., and Patterson, K., "Narrowband rejection of reaction wheel and environmental disturbances for the WFIRST OMC testbed," Guidance, navigation, and control, Vol 159, pp 251-262, (2017)

[9] Patterson, K., Shields, J., Wang, X., Tang, H., Azizi, A., Brugarolas, P., Mandic, M., and Shi, F., "Control Design for Momentum-Compensated Fast Steering Mirror for the WFIRST-AFTA Coronagraph Instrument," Proc. SPIE **9605**, pp. 9605-83, (2015).

[10] Shi; F. Cady, E. Seo, B-J., An, X., Balasubramanian, K., Kern, B., Lam, R., Marx, D., Moody, D., Prada, C. M., Patterson, K., Poberezhskiy, I., Shields, J., Sidick, E., Tang, H., Trauger, J., Truong, T., White, V., Wilson, D., Zhou, H., "Dynamic testbed demonstration of WFIRST coronagraph low order wavefront sensing and control (LOWFS/C),", SPIE **10400**, 10400-13, (2017)

[11] Cady, E., Balasubramanian, K., Gersh-Range, J., Kasdin, J., Kern, B., Lam, R., Prada, C. M., Moody, D., Patterson, K., Poberezhskiy, I., Riggs, A. J., Seo, B.-J., Shi, F., Tang, H., Trauger, J., Zhou, H., Zimmerman, N., "Shaped pupil coronagraphy for WFIRST: high-contrast broadband testbed demonstration," Proc. SPIE **10400**, 10400-14, (2017).

[12] Seo, B.-J., Cady, E., Gordon, B., Kern, B., Marx, D., Moody, D, Muller, R., Patterson, K., Poberezhskiy, I., Shi, F., Sidick, E., Trauger, J., and Wilson, D., "Hybrid Lyot coronagraph for WFIRST: high-contrast broadband testbed demonstration," Proc. SPIE **10400**, 10400-15, (2017).

[13]] Seo, B.-J., Balasubramanian, K., Cady, E., Gordon, B., Lam, R., Marx, D., Moody, D., Muller, R., Patterson, K., Poberezhskiy, I., Prada, C.M., Riggs A.J., Shi, F., Trauger, J., Wilson, D., "Hybrid Lyot coronagraph for WFIRST: high contrast testbed demonstration in flight-like environment," Proc. SPIE **10698**, 10698-95, (2018)

[14] Cox, A.N., "Allen's Astrophysical Quantities", Edition 4, (2002)

[15] Demers, R., "Review and update of WFIRST coronagraph instrument design and Technology," Proc. SPIE 10698, 10698-89, (2018)